

In-plane strain tuning multiferroicity in monolayer van der Waals NiI₂

Xiao-sheng Ni,¹ Dao-Xin Yao,^{1,*} and Kun Cao^{1,†}

¹Center for Neutron Science and Technology, Guangdong Provincial Key Laboratory of Magnetoelectric Physics and Devices, State Key Laboratory of Optoelectronic Materials and Technologies, School of Physics, Sun Yat-Sen University, Guangzhou, 510275, China

Multiferroic order with the engineered levels of strain in monolayer NiI₂ is explored based on density functional theory calculations and Monte Carlo simulations. Through the investigation of strain-free monolayer NiI₂, we find that the first nearest neighbor and third nearest neighbor exchange interactions play an essential role in the formation of its magnetic phase diagrams. The competition of these interactions induces magnetic frustration, leading to the formation of proper-screw helimagnetic ground state. We further show that these conclusions drawing from the strain-free monolayer can be well generalized to the cases within our engineered range of strains. Notably, our calculations show that with 6% tensile strain on the *a*-axis and 8% compressive strain on the *b*-axis, the Néel temperature T_N can be significantly enhanced to 101 K, about 5 times larger than that of the strain-free one. The strength of spontaneous electric polarizations can also be more than doubled under 8% uniform compressive strain on both axis. Our work suggests that strain is a promising way to tune multiferroic orders in the monolayer NiI₂, with the potential to significantly promote its transition temperatures and electric polarizations, therefore broaden the prospect of its applications in spintronics devices.

I. INTRODUCTION

Van der Waals (vdW) two-dimensional (2D) materials have attracted tremendous attention as they host novel properties in atomically thin systems, creating a wide area for fundamental research and potential applications [1, 2]. Many novel quantum phenomena, such as superconductivity, topological order and anomalous quantum Hall effect, which are promising in future quantum technologies, have also been found in vdW materials [3–6]. Among them, vdW materials with intrinsic magnetic and ferroelectric orders down to atomically thin layers, have received special attention, due to their potential to provide valuable platforms for the realization of nanoscale electronic devices [7, 8], such as spin field-effect transistors [9, 10] and ferroelectric random access memories [11–15]. Especially, vdW materials with intrinsic type-II multiferroicity, whose inversion symmetry is broken by magnetic orders, have created new opportunities to not only explore novel mechanisms of magnetoelectric coupling in 2D [16], but also construct multifunctional electronic devices.

Transition-metal dihalides MX₂ (where M is a transition metal and X is a halogen) is a class of vdW material with many multiferroic members, such as NiBr₂, MnI₂, CoI₂ and NiI₂ [17, 18]. Among them, NiI₂, a typical transition-metal dihalides with helical magnetic structures [19], has attracted a lot of researchers to study its magnetic properties [20–22]. After type-II multiferroic ground state been confirmed in bulk NiI₂ [23], great efforts have been made to study its magnetic and ferroelectric properties in few layers form. Ju *et al.* demonstrated

that the NiI₂ has a multiferroic state with a helical spin order even down to bilayer [24]. More recently, convincing evidence of the existence of multiferroic order in NiI₂ monolayer has been reported below a transition temperature ~ 21 K [16]. Fumega *et al.* then studied the free-standing NiI₂ monolayer based on *ab initio* calculations and revealed a locking between its helimagnetic and ferroelectric orders. However, the low transition temperature and weak ferroelectricity hinder its future applications in multifunctional devices. Strain engineering has been proven a powerful tool to tune properties of 2D materials, such as in CrI₃ [25], Fe₃GeTe₂ [26], and CrTe₂ [27]. By varying applied strains, such as epitaxially growing monolayer NiI₂ on different substrates, we may manipulate its structure and magnetic orders to promote the multiferroic transition temperatures and electric polarizations.

In this work, we study the multiferroic order of free-standing monolayer NiI₂ with engineered levels of strain using density functional theory (DFT) calculations and Monte Carlo (MC) simulations. Through the investigation of strain-free monolayer NiI₂, we find that the first nearest neighbor (NN) and third NN exchange interactions play an essential role in the formation of its magnetic phase diagrams. The competition of these interactions induces magnetic frustration, leading to the formation of proper-screw helimagnetic (HM) ground state. We further show that these conclusions drawing from the strain-free monolayer can be well generalized to the cases within our engineered range of strains. Notably, our calculations show that with 6% tensile strain on the *a*-axis and 8% compressive strain on the *b*-axis, the Néel temperature T_N can be significantly enhanced to 101 K, about 5 times higher than that of the strain-free one. The strength of spontaneous electric polarizations can also be more than doubled under 8% uniform compressive strain on both axes. Moreover, we construct a NiI₂ (monolayer)/Graphene (bilayer) heterostructure to sim-

* yaodaax@mail.sysu.edu.cn

† caok7@mail.sysu.edu.cn

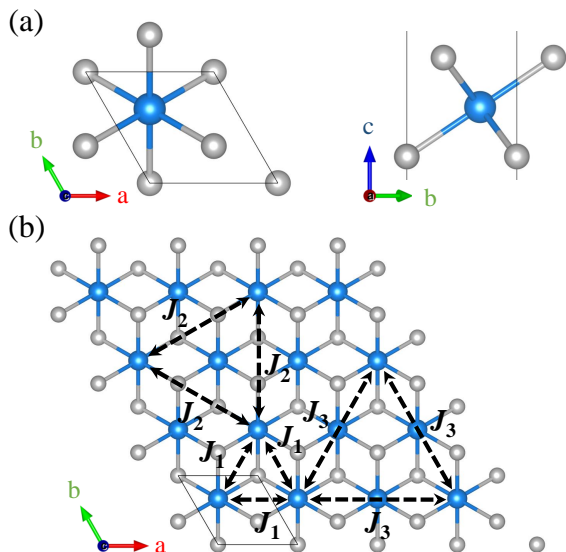


FIG. 1. (a) Side and top view of monolayer NiI_2 in a primitive cell. Blue and gray spheres represent Ni and I atoms, respectively. (b) The exchange paths are shown in black dotted line with arrows.

ulate a more realistic strain engineering and obtain results in good agreement with that from our calculations on corresponding freestanding one. Our work suggests that strain is a promising way to tune multiferroic orders in the monolayer NiI_2 , with the potential to significantly promote its transition temperatures and electric polarizations, therefore broaden the prospect of its applications in spintronics devices.

II. METHODS

First-principles calculations are carried out with the Vienna *ab initio* Simulation Package (VASP) [28, 29]. We use the Perdew Burke-Ernzerhof functional with a spin-polarized generalized gradient approximation (GGA). The projector augmented-wave (PAW) [30] method with a 500 eV plane wave cutoff is employed, and a $20 \times 20 \times 4$ Γ -centered k-point mesh allows the calculations to converge well. A vacuum layer thickness of 15 Å along the out-of-plane direction is used to avoid interaction between adjacent atomic layers. The spin-polarized GGA is combined with onsite Coulomb interactions, U , included for Ni $3d$ orbitals (GGA + U) [31]. We employ $U = 4$ eV and $J = 1$ eV, which achieves values of the magnetic moments and band gap consistent with experiments [32, 33]. Upon applying strain, we relax the crystal structure until the forces acting on each atom are less than 1 meV/Å. We determine the values of Heisenberg exchange interactions by fitting all J parameters to energies calculated by DFT using 20 randomly generated collinear magnetic configurations [34–36]. In-plane strain is defined as $\frac{a-a_0}{a_0} \times 100\%$ where a_0 and a denote lattice constants before and

after applying strain. Moreover, we consider the strains within $[-8\%, 8\%]$, which are sampled with an interval of 1% strain along each direction. For convenience, x and y are used to denote the strain level applied on the a -axis and b -axis, respectively. Electric polarizations are calculated using the Berry phase method [37]. The full atomic relaxation for all atoms in the heterostructure takes into account the vdW force through DFT-D3 method of Grimme [38]. Based on the calculated magnetic exchange interactions, we then explore the magnetic phase diagrams by a replica-exchange MC method [39]. The helical magnetic orders and corresponding magnetic propagation vectors \mathbf{Q} are identified by performing Fourier analysis on the magnetic configurations produced from MC simulations.

III. RESULTS AND DISCUSSIONS

A. Strain-free monolayer NiI_2

Bulk NiI_2 has the space group $R\bar{3}m$ (No. 166) with experimental lattice constants $a = b = 4.46$ Å and $c = 10.73$ Å [16, 40]. Experiments confirm that a HM state coexists with spontaneous electric polarization in the bulk NiI_2 when temperature drops below $T_N = 59.5$ K, with a HM propagation vector $\mathbf{Q} = (0.138, 0, 1.457)$ [19]. The monolayer NiI_2 , which could be potentially exfoliated from a bulk NiI_2 , has a reduced lattice symmetry with $P\bar{3}m1$ (No.164) [41]. As shown in Fig. 1(a), the monolayer NiI_2 is constructed by sandwiching one layer of Ni atoms between two layers of I atoms, where the three nearest Ni atoms form an equilateral triangle, with each Ni centred at a NiI_6 octahedron. For magnetic structures, although a nearest neighbour ferromagnetic (FM) interaction is expected from a 92° Ni-I-Ni bond angle according to the Goodenough-Kanamori rule [42], both experimental and theoretical studies show that a HM state is more stable in the bulk NiI_2 [19, 43] and even in the few-layers form [16, 40], suggesting that a HM ground state is also likely in the monolayer.

We utilize the classic Heisenberg model to describe the magnetic interactions in freestanding monolayer NiI_2 [44, 45],

$$H = \sum_{ij} J_{ij} \mathbf{S}_i \cdot \mathbf{S}_j - \sum_i (\mathbf{D} \cdot \mathbf{S}_i)^2 \quad (1)$$

where J_{ij} are exchange interactions between Ni spins \mathbf{S}_i and \mathbf{S}_j . The term with \mathbf{D} represents the magnetic anisotropy energy (MAE). We only consider exchange interactions with Ni-Ni bond lengths less than 10 Å. Because of the preservation of three-fold rotation axis in the strain-free case, there are only three types of nonequivalent exchange interactions, labeled as J_1 , J_2 and J_3 , as shown in Fig. 1(b). Our DFT calculations produce J_1 , J_2 and J_3 as -4.52 meV, -0.21 meV and 3.92 meV, respectively. The \mathbf{D} are calculated to be (0, 0, 0.39) meV,

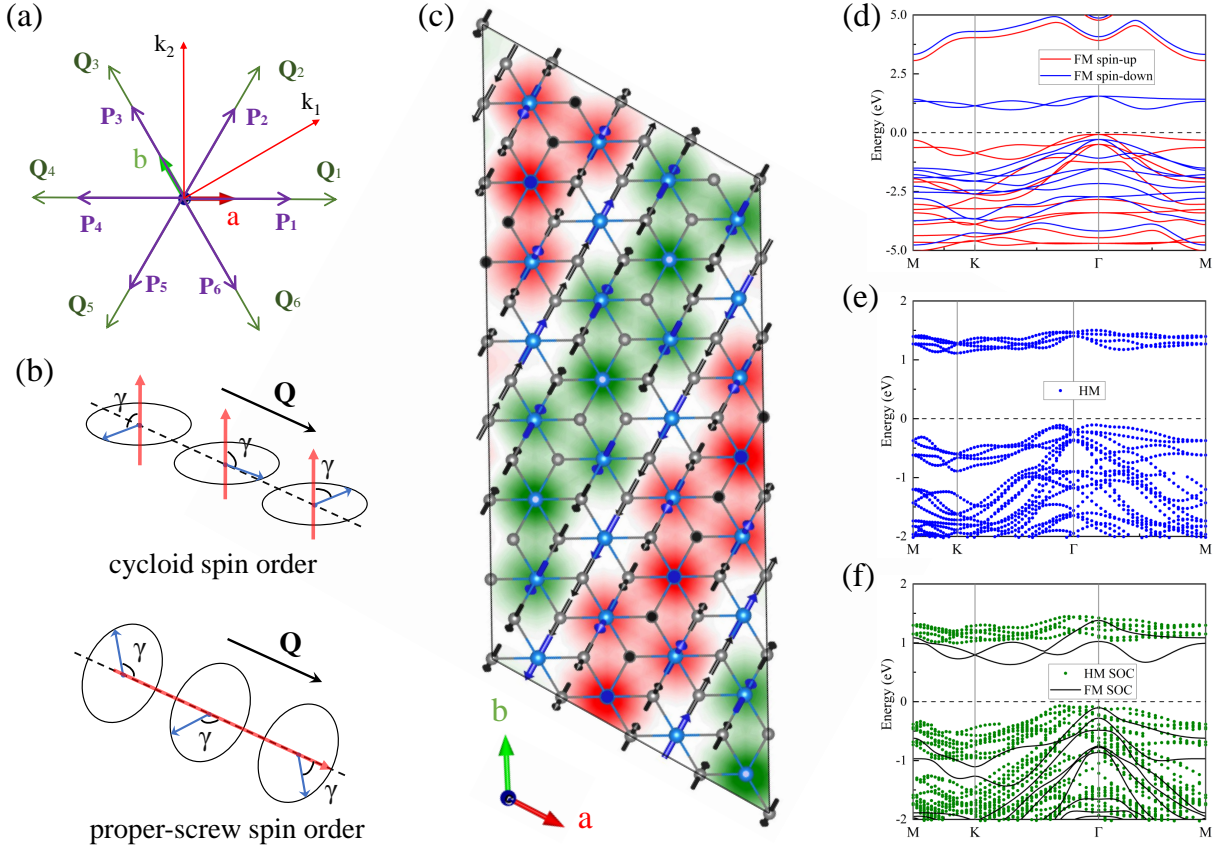


FIG. 2. (a) Schematic of the directions of \mathbf{Q} and electric polarization \mathbf{P} in real space. (b) The schematic of the cycloid and proper-screw magnetic order. (c) Illustration of the $\mathbf{Q}_1 = (0.25, -0.125, 0)$ HM state, where the large blue arrows and small black arrows represent the spin of Ni and I atoms respectively. The colour map shows the out-of-plane spin component with red and green denoting spin-up and spin-down respectively. (d)-(e) The band structures of monolayer NiI_2 in FM and HM states folded back into a primitive cell calculated without SOC. (f) The Band structure of FM and HM states with SOC.

corresponding to an MAE ~ 0.15 meV/Ni with an easy axis along the c direction. Evidently, the MAE is too weak to affect the T_N , as well as the magnetic vectors of the HM states, therefore for simplicity, we first analyse the ground state magnetic structures without considering MAE.

In the absence of MAE, a spin rotation axis in HM state can be generally assumed to be along the c direction and then each spin value in the monolayer NiI_2 can be determined by

$$\begin{aligned} \mathbf{S}_{n,0} = & S_0 \cdot (\cos(\mathbf{Q} \cdot (\mathbf{R}_n + \mathbf{R}_0)) \sin(\gamma)) \mathbf{a} \\ & + S_0 \cdot (\sin(\mathbf{Q} \cdot (\mathbf{R}_n + \mathbf{R}_0)) \sin(\gamma)) \mathbf{b} \\ & + \cos(\gamma) \mathbf{c} \end{aligned} \quad (2)$$

where S_0 is the magnitude of each spin, \mathbf{R}_n is the lattice vector pointing from the unit cell 0 to unit cell n , \mathbf{R}_0 is the position of the spin at origin, γ is the cone angle between the rotation axis and the magnetic moment of each atoms.

Denoting $\mathbf{Q} = (q_a, q_b, 0)$, the magnetic Hamiltonian in

a primitive cell can then be explicitly written as

$$\begin{aligned} H_{iso} = & J_1 S_0^2 \sin^2(\gamma) (\cos(q_a) + \cos(q_b) + \cos(q_a + q_b)) \\ & + J_2 S_0^2 \sin^2(\gamma) (\cos(2q_a + q_b) + \cos(q_a + 2q_b) \\ & \quad + \cos(q_a - q_b)) \\ & + J_3 S_0^2 \sin^2(\gamma) (\cos(2q_a) + \cos(2q_b) \\ & \quad + \cos(2q_a + 2q_b)) \\ & + (J_1 + J_2 + J_3) S_0^2 \cos^2(\gamma) \end{aligned} \quad (3)$$

By performing derivation of Eq. (3) with respect to q_a and q_b , we can find the corresponding magnetic ground state.

$$\frac{\partial H_{iso}}{\partial q_a} = 0 \quad \& \quad \frac{\partial H_{iso}}{\partial q_b} = 0 \quad (4)$$

By solving Eq. (4), we get the relation

$$q_a, q_b \sim \arctan\left(\left(\frac{J_1 + 3J_2 + 4J_3}{J_2 - J_1 + 4J_3}\right)^{1/2}\right) \quad (5)$$

From Eq. (5), we can see that the solutions of q_a and q_b

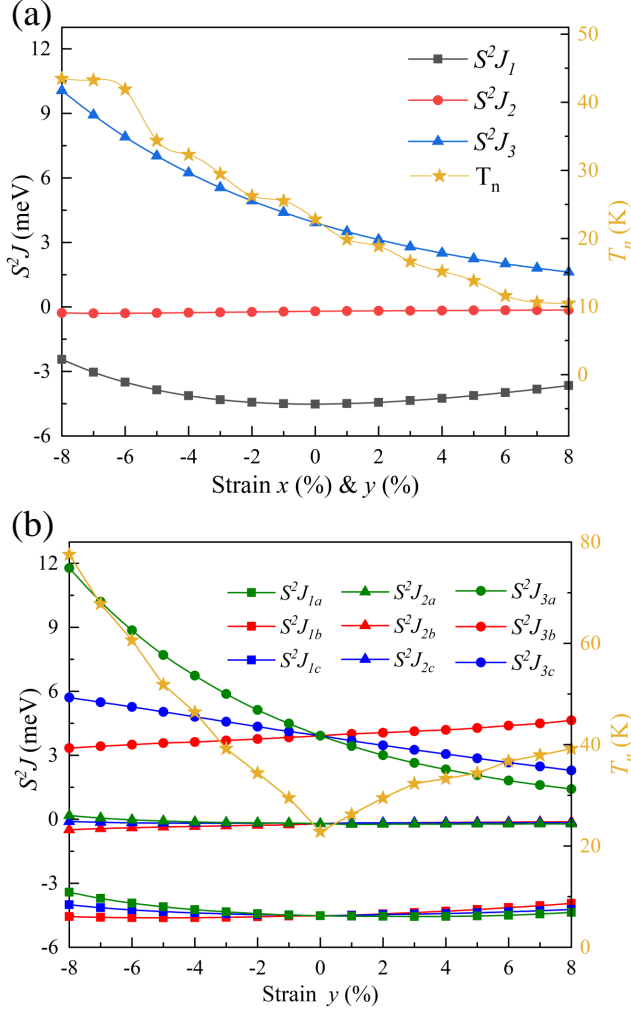


FIG. 3. (a) The magnetic exchange interactions J_1 , J_2 , J_3 , and the Néel temperature T_N with uniform strains. (b) The J_{1a-1c} , J_{2a-2c} , J_{3a-3c} and T_N as functions of y , with $x = 0\%$.

only exist when

$$\frac{J_1 + 3J_2 + 4J_3}{J_2 - J_1 + 4J_3} > 0 \quad (6)$$

Our calculated J 's fulfill the requirement of Eq. (6), suggesting that the ground state of monolayer NiI_2 should be HM. Evidently, frustration from the strong FM J_1 and the AFM J_3 are the main driving force for the formation of the HM state, while J_2 is too weak to qualitatively contribute. MC simulations with the calculated parameters are then performed, confirming the presence of a single phase transition from a paramagnetic phase to a HM phase, with a $T_N = 22.81$ K, in good agreement with the experimental result of 21 K [16]. The HM state possesses a single \mathbf{Q} , which has six symmetrically equivalent values (see Fig. 2(a)), confirmed by Fourier analysis on the spin configurations output by the MC simulations. All six \mathbf{Q} are along C_2 axis of monolayer NiI_2 , i.e. [100], [010] and [110] directions, with $|\mathbf{Q}| = 0.216 (2\pi)/a$ (see

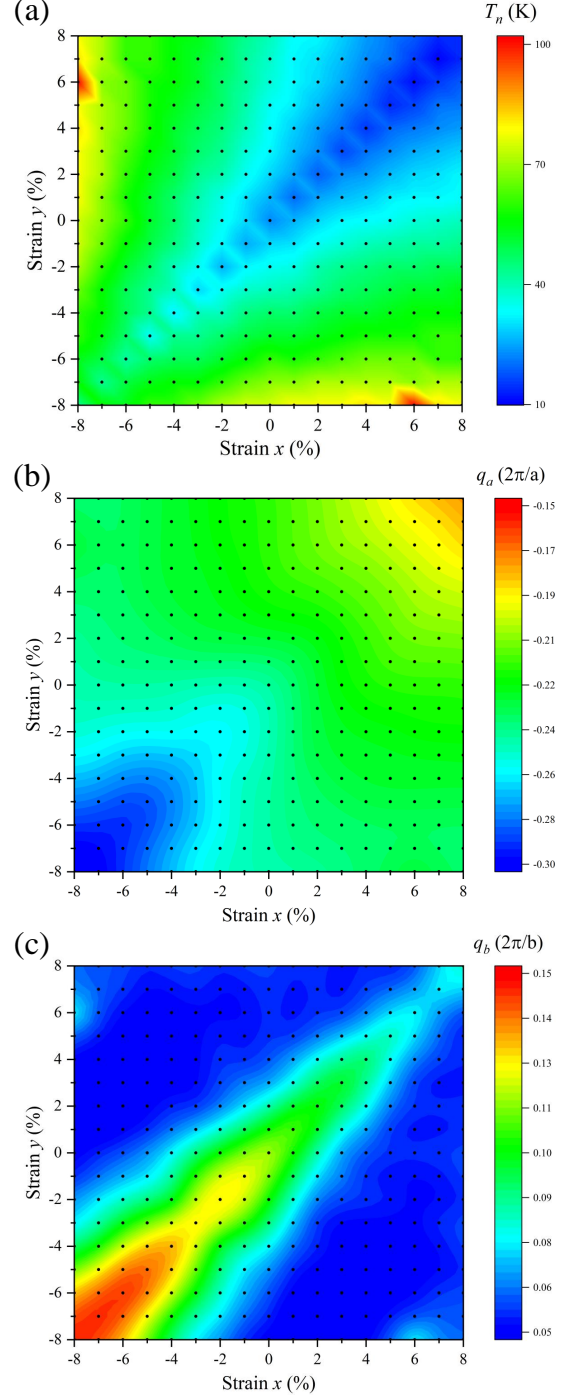


FIG. 4. (a) T_N as a function of lattice constants a and b , where the dark spots represent sampled strain points. (b)-(c) The q_a and q_b component of HM spin vector \mathbf{Q} as a function of lattice constants a and b .

Fig. 2(a)). The two-component \mathbf{Q} 's are distinct from that used in literatures, where the in-plane component (0.138, 0, 0) of the experimental \mathbf{Q} of the bulk NiI_2 is simply assumed [44]. To double check our model against DFT calculations, we further performed calculations on cycloid magnetic structures using the generalized Bloch

TABLE I. Values (in meV) of magnetic exchange couplings and T_N by DFT calculation and MC simulations in three typical strains.

$x(a\text{-axis})$ & $y(b\text{-axis})$ strain	J_{1a}	J_{1b}	J_{1c}	J_{2a}	J_{2b}	J_{2c}	J_{3a}	J_{3b}	J_{3c}	$T_N(\text{K})$
7% & 8%	-3.74	-3.73	-3.74	-0.14	-0.14	-0.16	1.83	1.70	1.59	13.77
7% & -3%	-4.02	-4.39	-4.60	-0.06	-0.16	-0.26	6.74	2.76	1.53	51.85
6% & -8%	-3.42	-4.25	-4.68	0.34	-0.05	-0.44	13.27	3.47	1.52	101.17

theorem. The results show that the total energy of our HM state is lower than the most stable single-component Q state.

The electric polarization \mathbf{P} of monolayer NiI_2 was reported to be parallel to the C_2 axis [16]. Given our calculated Q values, which are also parallel to the C_2 axis (see also illustration in Fig. 2(a)), the measured \mathbf{P} is expected to correspond to proper-screw HM states, according to symmetry arguments and calculations in isostructural MnI_2 [46]. However, our model can not distinguish a cycloid from a proper-screw order (see Fig. 2(b)). We thus again resort to direct DFT calculations. Without losing generality, we focus on the case with $\mathbf{Q}_1 = (0.25, -0.125, 0)$, which can be simulated using a $4 \times 8 \times 1$ supercell for both cycloid and proper-screw HM case. DFT calculations show that the proper-screw HM state is energetically more stable with 11.67 meV lower than the cycloidal one. We therefore propose that the magnetic ground state of monolayer NiI_2 is a proper-screw HM state. It is worth noting that the I atoms are also calculated to develop sizable magnetizations about $0.20 \mu_B$, forming a proper-screw HM state in coordination with that formed by the Ni spins (see Fig. 2(c)). Furthermore for ferroelectricity, we obtain an estimation of the polarization with an amplitude $|\mathbf{P}| \sim 2.62 \times 10^{-13} \text{ Cm}^{-1}$, with directions parallel to each Q (see Fig. 2(a)).

We further systematically investigate the electronic structure of monolayer NiI_2 . For comparison, the band structure of the FM state without SOC is first calculated. As shown in Fig. 2(d), the band gap is 3.13 eV for the spin-up channel and 1.27 eV for the spin-down channel, respectively. This significant difference between the two band gaps indicates that the FM monolayer NiI_2 is a half-semiconductor [47, 48], which has great potential for spintronic applications [49]. The conduction band minimum (CBM) is composed of spin-down states only, while the valence band maximum (VBM) is composed of spin-up states, leading to an overall band gap of 1.05 eV in the FM monolayer NiI_2 . However, the band gap in the FM state with SOC decreases to 0.73 eV. We further use a $4 \times 8 \times 1$ supercell to calculate the HM state with $\mathbf{Q}_1 = (0.25, -0.125, 0)$, with the bands unfolded to the Brillouin zone of a primitive cell [50]. As shown in Fig. 2(e), without SOC, the monolayer NiI_2 with the HM state is calculated to have a 1.23 eV indirect band gap near the Γ point. When SOC is considered, the CBM moves downward, leading to a slightly smaller gap (Fig. 2(f)). This overall semiconducting nature of the HM state provides a prerequisite for the appearance of spontaneous electric

polarization in the monolayer NiI_2 .

B. Strain engineered monolayer NiI_2

We firstly investigate the case of applying uniform biaxial strain, i.e., the same strain on both the a -axis and b -axis, to gain an insight about how strain generally affect the atomic structure and exchange interactions, hence the magnetic ordering. In this case, the original lattice symmetry is preserved. With the strain changed from -8% to 8%, the bond lengths of J_1 , J_2 and J_3 extend from 3.66 Å to 4.30 Å, 6.34 Å to 7.44 Å, 7.32 Å to 8.59 Å, respectively. Fig. 3(a) shows the evolution of the magnetic exchange interactions with the strain level x . It can be seen that J_1 keeps ferromagnetic, showing only slight variations. In contrast, although the J_3 remains antiferromagnetic, it decreases dramatically and monotonously with the increase of x , exhibiting much more tunability. Meanwhile, J_2 remains negligibly close to 0 throughout the whole range of x , therefore Eq. (6) can be simplified as

$$\frac{J_1}{J_3} > -4 \quad (7)$$

Our calculated ratio of J_1 and J_3 ranges from -2.25 to -0.24, satisfying Eq. (7), therefore suggests that the ground states remain HM under these strains.

To further explore the impact of different kind of strains on magnetic interactions, we now consider the case of uniaxial strains, i.e., zero strain on the a -axis combined with varying strain levels y on the b -axis. The J_1 , J_2 and J_3 now split into J_{1a-1c} , J_{2a-2c} and J_{3a-3c} respectively, due to a reduced lattice symmetry. In Fig. 3(b), it can be seen that J_{1a-1c} and J_{2a-2c} are overall not sensitive to the strains, similar to the behavior of their counterparts in the uniform strain case. Exceptionally, J_{3a-3c} behave differently among each other, with the J_{3a} showing significantly higher tunability, inheriting the characteristic of J_3 . Particularly, under maximum tensile strain with $y = -8\%$, although only small variation in the J_{3a-3c} bond length is induced, J_{3a} becomes over 4 times larger than J_{3b} (see Fig. 3(b)).

We now turn to arbitrary strains with unequal x and y ($-8\% \leq x, y \leq 8\%$). We find that in all scenarios, the calculated J 's behave similarly as been shown in Fig. 3(a)-(b), with only J_3 varies significantly with x and y . Importantly, the magnetic ground states are all

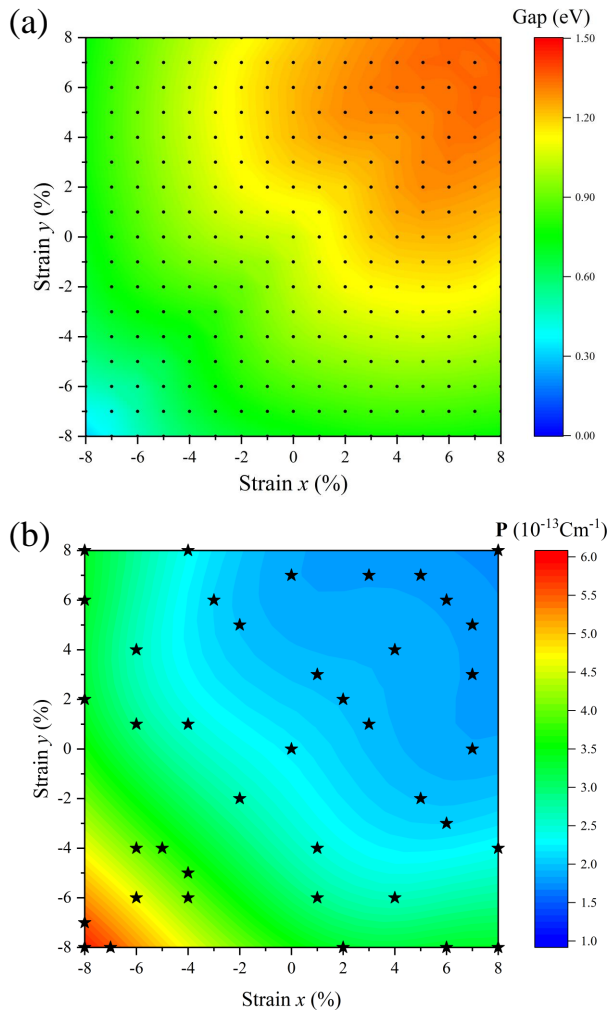


FIG. 5. (a) Band gap of the FM NiI_2 monolayer as a function of lattice constants a and b , where the dark spots represent sampled strain points. (b) The polarization of monolayer NiI_2 in proper-screw HM states as a function of lattice constants a and b , where the the dark stars are data points form the supercell calculation.

predicted to be HM according to the Eq. (7). With the calculated J 's, we further perform MC simulations for all sampled strains, with calculated T_N shown in Fig. 4(a). The corresponding color map is plotted to be symmetrical with respect to the diagonal line since the a -axis and b -axis are equivalent. Notably, the T_N exhibits dramatic variations, dropping with the increasing of tensile strains, down to 10.45 K at $x = 8\%$ and $y = 8\%$. Surprisingly, the T_N rises to 101.17 K with the $x = -8\%$ and $y = 6\%$, which is the highest among all our sampled cases, almost 5 times higher than that of the strain-free one. By examining the corresponding J 's, we find that the T_N largely evolves following the trend of the J_3 , and in the case of lowered symmetry, J_{3a} , which is the exchange interaction with the highest tunability (see Fig. 3(a)-(b) and Table. I for typical strain cases). We then further iden-

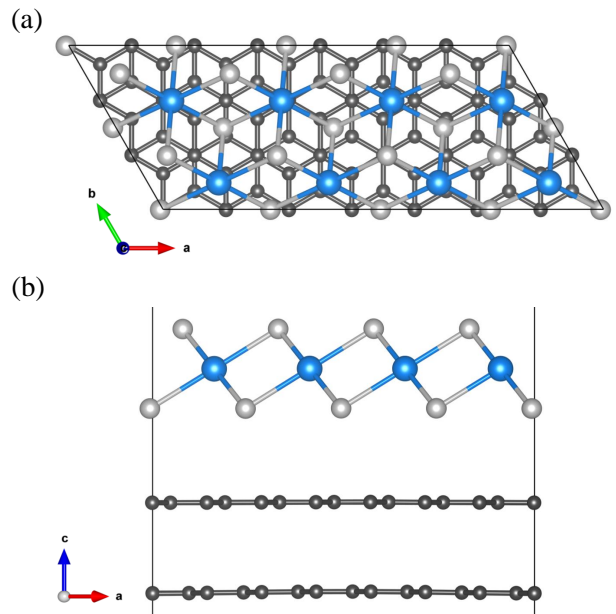


FIG. 6. (a)-(b) The top and side view of $4 \times 2 \times 1$ NiI_2 (monolayer)/ $7 \times 3 \times 1$ graphene (bilayer) heterostructures.

tify the HM propagation vectors \mathbf{Q} from the outputted spin configurations of MC simulations, with q_a and q_b shown in Fig. 4(b)-4(c) respectively. It can be seen that the amplitude of q_a are enlarged with the increasing tensile strains, while the q_b increases with the compressive strains (the diagonal lines of the color maps).

Once the \mathbf{Q} values are confirmed, we construct supercells to accommodate corresponding proper-screw spiral states to study their ferroelectricity. Since the supercell calculations are expensive, to reduce computational effort, we only perform supercell calculations on selected representative strain values, shown as stars in Fig. 5(b). We find that all the selected HM states have larger band gaps than that of the corresponding FM states. Therefore, to have a full sampling, band gaps of FM states with all strains are calculated and shown as a color map in Fig. 5(a). It can be seen that in all cases, the band gaps are finite, ranging from 0.30 eV to 1.36 eV, which increase with tensile strains and reduce with compressive strains, consistent with the general text-book physical picture. These band gaps guarantee that the HM ground states under the whole strain range are possible to sustain spontaneous electric polarizations. The electric polarizations \mathbf{P} are then calculated, with their amplitude $|\mathbf{P}|$ interpolated to a diagram in the strain map. As can be seen in Fig. 5(b), $|\mathbf{P}|$ keeps the same order in the whole strain range, with their behavior closely resembling that of the band gaps, but in an opposite way, which is quite evident from the comparison of Fig. 5(a) and Fig. 5(b). Therefore, the main driving force for the enhancement of $|\mathbf{P}|$ is the corresponding shrinking of the bang gap, although with compressive strains, the surface of the monolayer NiI_2 also contracts. For instance, with the maximum

TABLE II. Values (in meV) of magnetic exchange couplings and T_N by DFT calculation and MC simulations. The freestanding monolayer NiI_2 is under $x = -7\%$ and $y = 8\%$ strain, where the NiI_2 layer in NiI_2/BLG heterostructure is taking similar compressive and tensile strains.

	J_{1a}	J_{1b}	J_{1c}	J_{2a}	J_{2b}	J_{2c}	J_{3a}	J_{3b}	J_{3c}	$T_N(\text{K})$
NiI_2 monolayer	-2.98	-4.18	-4.58	0.08	-0.15	-0.20	12.38	2.49	1.02	71.07
NiI_2/BLG heterostructure	-3.50	-4.27	-4.51	0.22	-0.09	-0.37	12.06	2.81	1.22	70.73

compressive strain $x = -8\%$ and $y = -8\%$, the surface area of the monolayer NiI_2 is reduced by 15 %, but $|\mathbf{P}|$ becomes more than two times larger than that of the strain-free case.

To check the reliability of applying strain by solely changing the lattice constants, we construct a $\text{NiI}_2/\text{graphene}$ heterostructure to simulate practical ex-axial strain engineering through substrate. Bilayer graphene (BLG) has been successfully used as substrates to grow 2D magnetic materials, such as monolayer CrTe_2 [51]. As shown in Fig. 6(a), the constructed NiI_2/BLG heterostructure is composed of a $4 \times 2 \times 1$ supercell of NiI_2 and a $7 \times 3 \times 1$ supercell of BLG. By fixing the lattice constants of the BLG, 7.24% compressive strain ($x = -7.24\%$) and 8.22% tensile strain ($y = 8.22\%$) are applied on the a -axis and b -axis of monolayer NiI_2 , respectively. The calculated magnetic exchange interactions J_{1a-1c} , J_{2a-2c} and J_{3a-3c} in this heterostructure are shown in Table. II, resulting in a HM ground state with a $T_N = 71.07$ K. In comparison, as shown in Fig. 4(a), our calculations of freestanding monolayer NiI_2 with strain values of $x = -7\%$ and $y = 8\%$ produces a $T_N = 70.73$ K (Table. II), with the corresponding J values very close to that from the heterostructures. This excellent agreement validates the high reliability of our predictions based on freestanding calculations.

IV. SUMMARY

In summary, we study the multiferroic order of freestanding monolayer NiI_2 with engineered levels of strain using DFT calculations and MC simulations. Through the investigation of strain-free monolayer NiI_2 , we find that the first NN and third NN exchange interactions play an essential role in the formation of its magnetic

phase diagrams. The competition of these interactions induces magnetic frustration, leading to the formation of proper-screw HM ground state. We further show that these conclusions drawing from the strain-free monolayer can be well generalized to the cases within our engineered range of strains. Notably, our calculations show that with 6% tensile strain on the a -axis and 8% compressive strain on the b -axis, the Néel temperature T_N can be significantly enhanced to 101 K, about 5 times larger than that of the strain-free one. The strength of spontaneous electric polarizations can also be more than doubled under 8% uniform compressive strain on both axes. Moreover, we construct a NiI_2 (monolayer)/Graphene (bilayer) heterostructure to simulate a more realistic strain engineering and obtain results in good agreement with that based on calculations on corresponding freestanding one. Our work suggests that strain is a promising way to tune multiferroic orders in the monolayer NiI_2 , with the potential to significantly promote its transition temperatures and electric polarizations, therefore broaden the prospect of its applications in spintronics devices.

V. ACKNOWLEDGMENTS

Work at Sun Yat-Sen University was supported by the National Key Research and Development Program of China (Grants No. 2018YFA0306001, 2017YFA0206203), and the Guangdong Basic and Applied Basic Research Foundation (Grants No. 2022A1515011618, No. 2019A1515011337), and the National Natural Science Foundation of China (Grants No. 92165204, No. 11974432), and the Shenzhen International Quantum Academy (Grant No. SIQA202102), Leading Talent Program of Guangdong Special Projects (201626003).

-
- [1] D. Jariwala, A. R. Davoyan, J. Wong, and H. A. Atwater, Van der Waals materials for atomically-thin photovoltaics: promise and outlook, *Acs Photonics* **4**, 2962 (2017).
- [2] B. Huang, G. Clark, E. Navarro-Moratalla, D. R. Klein, R. Cheng, K. L. Seyler, D. Zhong, E. Schmidgall, M. A. McGuire, D. H. Cobden, *et al.*, Layer-dependent ferromagnetism in a van der Waals crystal down to the monolayer limit, *Nature* **546**, 270 (2017).
- [3] R. Bian, C. Li, Q. Liu, G. Cao, Q. Fu, P. Meng, J. Zhou, F. Liu, and Z. Liu, Recent progress in the synthesis of novel two-dimensional van der Waals materials, *National Science Review* **9**, nwab164 (2022).
- [4] Y. Deng, Y. Yu, M. Z. Shi, Z. Guo, Z. Xu, J. Wang, X. H. Chen, and Y. Zhang, Quantum anomalous Hall effect in intrinsic magnetic topological insulator MnBi_2Te_4 , *Science* **367**, 895 (2020).

- [5] J. Wu, F. Liu, M. Sasase, K. Ienaga, Y. Obata, R. Yukawa, K. Horiba, H. Kumigashira, S. Okuma, T. Inoshita, *et al.*, Natural van der Waals heterostructural single crystals with both magnetic and topological properties, *Science advances* **5**, eaax9989 (2019).
- [6] J. Li, P. Song, J. Zhao, K. Vaklinova, X. Zhao, Z. Li, Z. Qiu, Z. Wang, L. Lin, M. Zhao, *et al.*, Printable two-dimensional superconducting monolayers, *Nature Materials* **20**, 181 (2021).
- [7] K. S. Burch, D. Mandrus, and J.-G. Park, Magnetism in two-dimensional van der Waals materials, *Nature* **563**, 47 (2018).
- [8] J.-G. Park, Opportunities and challenges of 2D magnetic van der Waals materials: magnetic graphene?, *Journal of Physics: Condensed Matter* **28**, 301001 (2016).
- [9] M. Bonilla, S. Kolekar, Y. Ma, H. C. Diaz, V. Kalappattil, R. Das, T. Eggers, H. R. Gutierrez, M.-H. Phan, and M. Batzill, Strong room-temperature ferromagnetism in VSe₂ monolayers on van der Waals substrates, *Nature nanotechnology* **13**, 289 (2018).
- [10] Z.-Z. Lin and X. Chen, Ultrathin scattering spin filter and magnetic tunnel junction implemented by ferromagnetic 2D van der Waals material, *Advanced Electronic Materials* **6**, 1900968 (2020).
- [11] B. Park, B. Kang, S. Bu, T. Noh, J. Lee, and W. Jo, Lanthanum-substituted bismuth titanate for use in non-volatile memories, *Nature* **401**, 682 (1999).
- [12] J. Scott, Applications of modern ferroelectrics, *science* **315**, 954 (2007).
- [13] S.-T. Han, Y. Zhou, and V. Roy, Towards the development of flexible non-volatile memories, *Advanced Materials* **25**, 5425 (2013).
- [14] C. Cui, W.-J. Hu, X. Yan, C. Addiego, W. Gao, Y. Wang, Z. Wang, L. Li, Y. Cheng, P. Li, *et al.*, Intercorrelated in-plane and out-of-plane ferroelectricity in ultrathin two-dimensional layered semiconductor In₂Se₃, *Nano letters* **18**, 1253 (2018).
- [15] S. Yuan, X. Luo, H. L. Chan, C. Xiao, Y. Dai, M. Xie, and J. Hao, Room-temperature ferroelectricity in MoTe₂ down to the atomic monolayer limit, *Nature communications* **10**, 1 (2019).
- [16] Q. Song, C. A. Occhialini, E. Ergeçen, B. Ilyas, D. Amoroso, P. Barone, J. Kapeghian, K. Watanabe, T. Taniguchi, A. S. Botana, *et al.*, Evidence for a single-layer van der Waals multiferroic, *Nature* **602**, 601 (2022).
- [17] K. F. Mak, J. Shan, and D. C. Ralph, Probing and controlling magnetic states in 2D layered magnetic materials, *Nature Reviews Physics* **1**, 646 (2019).
- [18] M. A. McGuire, Crystal and magnetic structures in layered, transition metal dihalides and trihalides, *Crystals* **7**, 121 (2017).
- [19] S. Kuindersma, J. Sanchez, and C. Haas, Magnetic and structural investigations on NiI₂ and CoI₂, *Physica B+C* **111**, 231 (1981).
- [20] M. Lu, Q. Yao, C. Xiao, C. Huang, and E. Kan, Mechanical, electronic, and magnetic properties of nix₂ (x= cl, br, i) layers, *ACS omega* **4**, 5714 (2019).
- [21] H. Liu, X. Wang, J. Wu, Y. Chen, J. Wan, R. Wen, J. Yang, Y. Liu, Z. Song, and L. Xie, Vapor deposition of magnetic van der Waals NiI₂ crystals, *ACS nano* **14**, 10544 (2020).
- [22] D. Amoroso, P. Barone, and S. Picozzi, Interplay between Single-Ion and Two-Ion Anisotropies in Frustrated 2D Semiconductors and Tuning of Magnetic Structures Topology, *Nanomaterials* **11**, 1873 (2021).
- [23] T. Kurumaji, S. Seki, S. Ishiwata, H. Murakawa, Y. Kaneko, and Y. Tokura, Magnetoelectric responses induced by domain rearrangement and spin structural change in triangular-lattice helimagnets NiI₂ and CoI₂, *Phys. Rev. B* **87**, 014429 (2013).
- [24] H. Ju, Y. Lee, K.-T. Kim, I. H. Choi, C. J. Roh, S. Son, P. Park, J. H. Kim, T. S. Jung, J. H. Kim, *et al.*, Possible persistence of multiferroic order down to bilayer limit of van der Waals material NiI₂, *Nano Letters* **21**, 5126 (2021).
- [25] T. Li, S. Jiang, N. Sivadas, Z. Wang, Y. Xu, D. Weber, J. E. Goldberger, K. Watanabe, T. Taniguchi, C. J. Fennie, *et al.*, Pressure-controlled interlayer magnetism in atomically thin CrI₃, *Nature materials* **18**, 1303 (2019).
- [26] Y. Wang, C. Wang, S.-J. Liang, Z. Ma, K. Xu, X. Liu, L. Zhang, A. S. Admasu, S.-W. Cheong, L. Wang, *et al.*, Strain-sensitive magnetization reversal of a van der waals magnet, *Advanced Materials* **32**, 2004533 (2020).
- [27] L. Wu, L. Zhou, X. Zhou, C. Wang, and W. Ji, In-plane epitaxy-strain-tuning intralayer and interlayer magnetic coupling in crse₂ and crte₂ monolayers and bilayers, *Phys. Rev. B* **106**, L081401 (2022).
- [28] G. Kresse and J. Hafner, Ab initio molecular dynamics for liquid metals, *Phys. Rev. B* **47**, 558 (1993).
- [29] G. Kresse and J. Furthmüller, Efficient iterative schemes for ab initio total-energy calculations using a plane-wave basis set, *Phys. Rev. B* **54**, 11169 (1996).
- [30] P. E. Blöchl, Projector augmented-wave method, *Phys. Rev. B* **50**, 17953 (1994).
- [31] A. I. Liechtenstein, V. I. Anisimov, and J. Zaanen, Density-functional theory and strong interactions: Orbital ordering in Mott-Hubbard insulators, *Phys. Rev. B* **52**, R5467 (1995).
- [32] A. L. Chen, P. Y. Yu, and R. D. Taylor, Closure of the charge-transfer energy gap and metallization of NiI₂ under pressure, *Phys. Rev. Lett.* **71**, 4011 (1993).
- [33] Q. Cui, J. Liang, B. Yang, Z. Wang, P. Li, P. Cui, and H. Yang, Giant enhancement of perpendicular magnetic anisotropy and induced quantum anomalous Hall effect in graphene/NiI₂ heterostructures via tuning the van der Waals interlayer distance, *Phys. Rev. B* **101**, 214439 (2020).
- [34] D. Morgan, B. Wang, G. Ceder, and A. van de Walle, First-principles study of magnetism in spinel MnO₂, *Phys. Rev. B* **67**, 134404 (2003).
- [35] N. S. Fedorova, C. Ederer, N. A. Spaldin, and A. Scaramucci, Biquadratic and ring exchange interactions in orthorhombic perovskite manganites, *Phys. Rev. B* **91**, 165122 (2015).
- [36] Z. Liu, X.-S. Ni, L. Li, H. Sun, F. Liang, B. A. Frandsen, A. D. Christianson, C. dela Cruz, Z. Xu, D.-X. Yao, J. W. Lynn, R. J. Birgeneau, K. Cao, and M. Wang, Effect of iron vacancies on magnetic order and spin dynamics of the spin ladder bafe_{2-δ}s_{1.5}se_{1.5}, *Phys. Rev. B* **105**, 214303 (2022).
- [37] R. D. King-Smith and D. Vanderbilt, Theory of polarization of crystalline solids, *Phys. Rev. B* **47**, 1651 (1993).
- [38] S. Grimme, J. Antony, S. Ehrlich, and H. Krieg, A consistent and accurate ab initio parametrization of density functional dispersion correction (DFT-D) for the 94 elements H-Pu, *The Journal of chemical physics* **132**, 154104 (2010).

- [39] K. Cao, G.-C. Guo, D. Vanderbilt, and L. He, First-principles modeling of multiferroic rmn_2O_5 , *Phys. Rev. Lett.* **103**, 257201 (2009).
- [40] H. Ju, Y. Lee, K.-T. Kim, I. H. Choi, C. J. Roh, S. Son, P. Park, J. H. Kim, T. S. Jung, J. H. Kim, *et al.*, Possible persistence of multiferroic order down to bilayer limit of van der Waals material NiI_2 , *Nano Letters* **21**, 5126 (2021).
- [41] Y. An, H. Wang, J. Liao, Y. Gao, J. Chen, Y. Wu, Y. Li, G. Xu, and C. Ma, Spin transport properties and nanodevice simulations of NiI_2 monolayer, *Physica E: Low-dimensional Systems and Nanostructures* **142**, 115262 (2022).
- [42] J. B. Goodenough, Goodenough-Kanamori rule, *Scholarpedia* **3**, 7382 (2008).
- [43] T. Kurumaji, S. Seki, S. Ishiwata, H. Murakawa, Y. Kaneko, and Y. Tokura, Magnetoelectric responses induced by domain rearrangement and spin structural change in triangular-lattice helimagnets NiI_2 and CoI_2 , *Physical Review B* **87**, 014429 (2013).
- [44] A. O. Fumega and J. L. Lado, Microscopic origin of multiferroic order in monolayer NiI_2 , *2D Materials* **9**, 025010 (2022).
- [45] D. Amoroso, P. Barone, and S. Picozzi, Spontaneous skyrmionic lattice from anisotropic symmetric exchange in a Ni-halide monolayer, *Nature communications* **11**, 1 (2020).
- [46] H. J. Xiang, E. J. Kan, Y. Zhang, M.-H. Whangbo, and X. G. Gong, General theory for the ferroelectric polarization induced by spin-spiral order, *Phys. Rev. Lett.* **107**, 157202 (2011).
- [47] Y. An, H. Wang, J. Liao, Y. Gao, J. Chen, Y. Wu, Y. Li, G. Xu, and C. Ma, Spin transport properties and nanodevice simulations of NiI_2 monolayer, *Physica E: Low-dimensional Systems and Nanostructures* **142**, 115262 (2022).
- [48] X.-j. Dong, M.-j. Ren, and C.-w. Zhang, Quantum anomalous hall effect in germanene by proximity coupling to a semiconducting ferromagnetic substrate NiI_2 , *Physical Chemistry Chemical Physics* **10.1039/D2CP02688K** (2022).
- [49] M. Boudjelal, A. Belfedal, B. Bouadjemi, T. Lantri, R. Bentata, M. Batouche, and R. Khenata, Ferromagnetic Half-Semiconductor (HSC) gaps in co-doped CdS: Ab-initio study, *Chinese Journal of Physics* **61**, 155 (2019).
- [50] W. Ku, T. Berlijn, and C.-C. Lee, Unfolding first-principles band structures, *Phys. Rev. Lett.* **104**, 216401 (2010).
- [51] J.-J. Xian, C. Wang, J.-H. Nie, R. Li, M. Han, J. Lin, W.-H. Zhang, Z.-Y. Liu, Z.-M. Zhang, M.-P. Miao, *et al.*, Spin mapping of intralayer antiferromagnetism and field-induced spin reorientation in monolayer CrTe_2 , *Nature communications* **13**, 1 (2022).